Microstructure and mechanical properties of friction stir welded AA6092/SiC metal matrix composite

Omar S. Salih[a,*], Hengan Ou[a,*], Xingguo Wei[b], W. Sun[a]

[a] Department of Mechanical, Materials and Manufacturing Engineering, University of Nottingham, Nottingham NG7 2RD, UK
[b] TWI Ltd. TWI Technology Centre (Yorkshire), Wallis Way, Catcliffe, Rotherham S60 5TZ, UK

ABSTRACT

There is a need for improved understanding on the effects of friction stir welding (FSW) on the metallurgical and mechanical properties of aluminium matrix composite (AMC). In this study, AA6092/SiC/17.5p-T6 AMC joints were produced by using FSW with varying tool rotation and traverse speeds. The microstructural characterisation by scanning electron microscopy equipped with electron backscattered diffraction (EBSD) system revealed a substantial grain refinement and a homogeneous distribution of reinforcement particles in the nugget zone. The grain size of the nugget zone was greatly influenced by weld pitch, as a key indicator to control the amount of heat input, exposure time and cooling rate. Vickers microhardness profile across the welding zone revealed a significant difference in microhardness among the base metal, heat affected zone, thermo-mechanically affected zone and nugget zone. The tensile strength of the cross-weld specimens showed a high joint efficiency of about 75% of the base metal combined with relatively high ductility. Low-cycle fatigue properties were investigated in the axial total strain-amplitude control mode (from 0.3% to 0.5%) with $R = \varepsilon_{min}/\varepsilon_{max} = -1$. The results indicate that the fatigue life of the cross-welded joints varies with grain size in the nugget zone and it is lower than that of the base metal. A significant improvement of fatigue life is found to be related to the finer equiaxed grains dominated by high angle grain boundaries in the nugget zone.

1. Introduction

Advanced materials like aluminium matrix composite (AMC) are considered to have considerable potential for lightweight applications due to their superior mechanical and physical properties at elevated and ambient temperature, compared to the unreinforced aluminium alloys [1]. AMCs reinforced with ceramic particles are more attractive than those of the other geometries of reinforcement such as flake and fibre, owing to their isotropic properties, oxidation resistance, higher operating temperature, and ease of fabrication [2]. However, the toughness of AMC in term of ductility and fracture toughness is lower than that of its matrix alloy [3]. Thus the improvement of the fatigue life of AMC is most pronounced in the high cycle fatigue (HCF) regime than in low cycle fatigue (LCF) as a result of ductility exhaustion [3–5]. Regarding the joining of AMC by the conventional welding process, it has been observed that there is a deleterious reaction between the molten metal and reinforcement particles with inhomogeneous redistribution of reinforcement particles frequently occurred in the fusion zone [6]. As a result, the weldability of AMC by fusion processes is limited, and the attractive mechanical properties of these materials

have yet to be entirely utilised [7,8].

As a solid-state thermo-mechanical joining technique, friction stir welding (FSW) is considered a promising technique for joining AMC. In FSW, the combination of heat, and high plastic strain involved during the welding process can produce finer grain and more homogeneous distribution of the reinforcement particles in the nugget zone (NZ) [9,10]. However, FSW of AMC is not an easy task, and significant challenges remain in achieving optimum welding window and sufficient mechanical properties [11].

In recent years, work has been reported in looking into the effect of FSW parameters on the metallurgical and mechanical properties of aluminium alloy (6xxx) as a base matrix reinforced with various ceramic particulates, including, AA6061/SiC [12,13], AA6061/B$_4$C [11,14], AA6061/ZrB$_2$ [15,16], AA6061/AlN [17], AA6061/Al$_2$O$_3$ [18,19], and AA6063/ B$_4$C [20]. Results showed that the welding parameters play a significant role to produce sound joints. Periyasamy et al. [12] reported that the tool rotation and traverse speeds influence the generated temperature in the NZ and subsequent metal flow and grain growth. Intermittent or turbulent metal flow characterises the stirring zone when insufficient or excessive heat input was used. Both of

---

these conditions produce defective welds, as the stirring rate of plasticised material determines defects formation in the NZ. Tunnel defect is more likely to happen at an excessive stirring rate, while lack of bonding is formed at an insufficient stirring rate [21], suggesting a narrower welding window of AMC than that for monolithic aluminium alloys. Also, the strength of FSW joints is significantly affected by welding parameters. The joints efficiency (JE) (the ratio of the ultimate tensile strength of joints to the ultimate tensile strength of the base metal (BM) of AMC joints was lower than the BM [13,14,17,21], which is resulted from the formation of coarse grains, lower hardness, and presence of defects.

Although effort has been focused on the effect of FSW parameters on the microstructure and corresponding tensile and hardness properties of 6xxxAl composite joints, the fatigue behaviour of the welded joints have been examined to a limited scope. In this context, Minak et al. [22] and Pirondi et al. [23] have reported the HCF properties and fatigue crack propagation of AA6061/Al$_2$O$_3$/22p FSW joints. They reveal that the fatigue behaviour of welded joints was dependent on the evolved microstructure in the NZ. Ceschini et al. [24] investigated the effect of the FSW process on the LCF of AA6061/Al$_2$O$_3$/20p FSW joints. A reduction in the fatigue life of FSW joints as compared to that of the BM has been observed as a result of surface roughness, and the induced plastic strain during welding. More recently, Ma et al. [25] identified in their critical reviews that insufficient investigations had been carried out focusing on the LCF behaviour FSW joints, although many of the envisaged applications for the AMCs undergo cyclic loading with high amplitude of strain and stress during service life resulting in fatigue damage and severely limit the useful life and the performance of the components [26]. Furthermore, the LCF in the composite metals may occur because of repeated localised yielding near stress raisers (strengthening particles) that lead to stress concentration, despite the bulk of the component under elastic deformation. Thus it remains an open question on how to improve the strength and fatigue behaviour of AMCs joints.

To this end, no work has been done on the FSW of AA6092/SiC/17.5p-T6. Thus this work aims to fill this gap and make a detailed assessment of the feasibility of FSW application for this alloy. The focus of the study is to investigate the effect of two most important FSW parameters (tool rotation and traverse speeds) on the thermal history and microstructural changes, and to evaluate the resultant mechanical properties using microhardness, tensile and LCF testing. The obtained results are elucidated in the light of the interaction between the welding parameters and the existing theoretical background.

2. Material and experimental procedures

The as-received AMC sheet is AA6092/SiC/17.5p-T6, manufactured by powder metallurgy technique and subsequently rolled into 3.1 mm thick sheets. An aluminium alloy of AA 6092 was used as a matrix reinforced by 17.5 wt%. of SiC particles with an average size of around 6 µm. Sheets having dimensions of 110 mm × 50 mm were welded parallel to the rolling direction at TWI Technology Centre (Yorkshire) by using a bespoke FSW machine, and a total of nine joints denoted as W1–W9 was performed as shown in Table 1.

The welding tool was manufactured from AISI H13 with 6° flat edge featureless concave shoulder of 16 mm in diameter and an M6 threaded

Table 1
Summary of welding matrix.

		Tool rotation speed (rpm)		
		1500	1800	2100
Tool traverse speed (mm/min)	25	W1	W4	W7
	50	W2	W5	W8
	100	W3	W6	W9

cylindrical pin having a length of 2.8 mm with a domed end. A plasma nitriding heat treatment was carried out to the tool to achieve a hardness of 950 Hv. The tool rotation axis was tilted by a 2° from the sheet normal and rotated anticlockwise, and the plunge depth was controlled to be ~0.05 mm, which means the depth of the shoulder into the top surface of the workpiece. The maximum welding temperature in the NZ was measured by FLIR infrared camera. Eight K-type thermocouples (TC) of 1.6 mm diameter were embedded on the retreating side (RS) (TC1-TC4) and the advancing side (AS) (TC5-TC8), 10 mm away from the weld centre and 3 mm between each other to measure the thermal distribution across the joints as shown in Fig. 1(a).

For microstructure examinations, samples were cut perpendicular to the welding direction (cross-welds) (Fig. 1(a)) then prepared according to the standard metallographic techniques for specimen preparation consisting of grinding with 220, 400, 800, 1200, 2000 and 4000 grit emery papers followed by cloth polishing with 6 and 1 µm diamond. Finally, BUEHLER vibratory polisher was used with 0.025 µm colloidal silica to obtain a high surface finish. The microstructure observations were carried out by high-resolution field emission gun scanning electron microscope (FEG-SEM; JEOL, 7100F) equipped with an Oxford electron-backscatter diffraction (EBSD) system operated at 15 kV with a step size of 0.25 µm and 70° stage tilt. A lower limit boundary misorientation angle cut off 3° was used to avoid spurious boundaries, and a 15° misorientation criterion was used to differentiate between low-angle grain boundaries (LAGBs) and high-angle grain boundaries (HAGBs).

For mechanical testing, cross-weld flat dog-bone tensile and LCF specimens were extracted from the FSW joints as shown in Fig. 1(a). In addition to this, one longitudinal tensile sample was extracted from the W3 FSW joint (WL3) (Fig. 1(b)) to compare the influence of the tensile strength along the longitudinal and transverse direction of the weld. The samples were then ground and polished parallel to the principal load direction to exclude the effect of stress concentration, and non-homogeneous distribution of thicknesses caused by the FSW. Tensile tests were performed on samples with a gauge width of 6 mm and length of 37 mm according to ASTM E8M-13a by an INSTRON 5581-50KN instrument at a constant strain rate of 1×10^{-4} s^{-1}, with an extensometer having a gage length of 25 mm. The LCF tests were carried out by INSTRON 8801-50KN servo-hydraulic test machine on specimens with a gauge width of 8 mm and length of 28 mm according to the BS ISO 12106:2017 in a fully reversed total strain-controlled condition (R = −1). The strain function exhibited triangular waveforms and the test conducted at a constant strain rate of 5×10^{-4} s^{-1} at ambient temperature with anti-buckling restraints. A strain amplitudes of 0.3–0.7% were used for the BM and 0.3–0.5% for cross-weld samples. An axial clip extensometer with a gage length of 12.5 mm was used to control the amount of applied strain, and the fatigue failure criteria were defined when the maximum tensile stress dropped by 30% below that at initial life. Vickers microhardness measurements were taken on the cross-weld by using a Buehler hardness tester with 100 gf load. An average of three hardness readings was taken at cross-weld; in the mid-thickness and above and under by 0.5 mm.

3. Experimental results

3.1. Welding temperature and thermal history

Fig. 2(a) shows the effect of welding parameters on the generated peak temperature in the NZ. As the tool rotation speed increased from 1500 to 2100 rpm at a constant tool traverse speed of 25 mm/min, the generated peak temperature increased from around 500–605 °C. On the other hand, the rises of traverse speed from 25 to 100 mm/min lead to a reduction of the peak temperature from about 500–488 °C at a constant tool rotation speed of 1500 rpm. There is no significant change in the welding temperature, and it tends to be saturated when the rotation speed rises from 1800 to 2100 rpm, this phenomenon was also
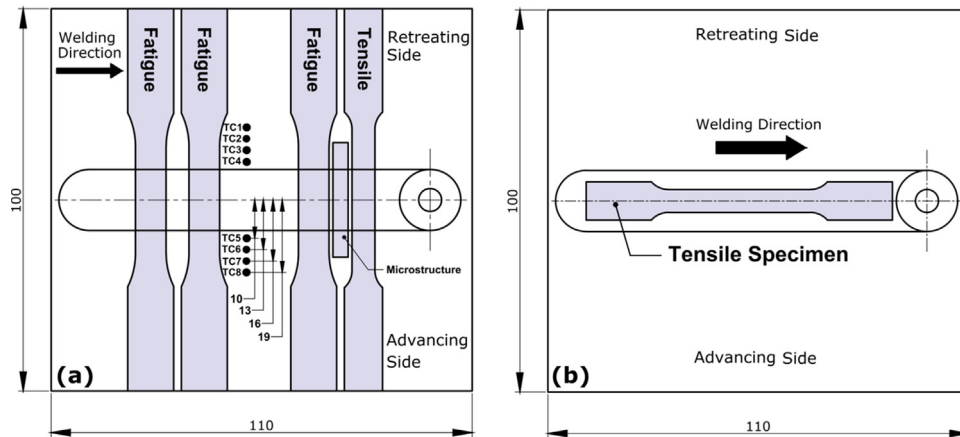
Fig. 1. (a) Illustration of friction stir welds and the positions of the thermocouples attached on the samples and the extraction of cross-weld testing sample locations, (b) the extraction of longitudinal tensile sample location from the weld (all dimensions in mm).

confirmed experimentally by Sato et al. [27]. This observation can be related to the reduction of the friction coefficient and torque when the weld metal softens at a high temperature, which leads to a reduction in heat generation by mechanical work and stabilises the temperature to avoid the melting of metal [28]. Fig. 2(b) compares the thermal history in the centre of NZ for W1, W3, W7, and W9 welds (corners of welding matrix). It is evident that the temperature gradient from the peak temperature of the NZ decreases with the reduction of traverse speed. The increase of traverse speed from 25 to 100 mm/min at a constant rotation speed of 1500 rpm reduces the cooling time from peak temperature from about 150 s to around 40 s, which indicates higher cooling rate [29]. Fig. 2(c) shows the typical thermal history measured in the AS and RS as a function of distance from the welding line for the joint welded at highest heat input (W7). The recorded temperature shows a nearly symmetric trend on both sides concerning the weld line. However, it is clear that the temperature at the RS (TC1-TC4) is higher than that at the AS (TC5-TC8); this behaviour is consistent with the study by Schneider [30], and can be attributed to the colder metal on the AS ahead of the tool with hot metals swept to the RS.

3.2. Metallurgical characterisation and microstructure evolution in the nugget zone

The surface morphologies of typical FSW joints fabricated by using tool rotation speeds of 1500 and 2100 rpm at constant tool traverse speed of 25 mm/min (W1 and W7) are shown in Fig. 3((a) and (b)). Visual observations revealed that a rough surface was formed at the lowest tool rotation speed of 1500 rpm (Fig. 3(a)), which is characteristic of too cold processing conditions [31]. Smoother surface with
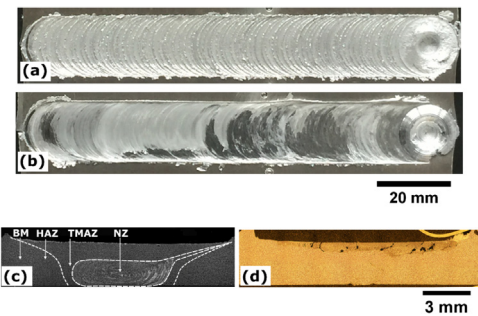

Fig. 3. (a, b) Surface morphologies of W1, and W7 FSW joints, (c) typical cross-weld macrostructure (W5), and (d) cross-weld macrostructure of W8. (AS on the right).

flash, however, occurs at the highest rotational speed of 2100 rpm (Fig. 3(b)), due to more softening of material with increasing rotational speed, in agreement with another author [31]. The typical cross-weld macrostructure of AA6092/SiC FSW joint (W5) is revealed in Fig. 3(c). It can be seen that the friction stir zone (FSZ) consists of three different zones, namely heat affected zone (HAZ), thermomechanically affected zone (TMAZ), and nugget zone (NZ) with an elliptical shape, which is identified explicitly in all joints, the same as that reported by Feng et al. [32], and Cavaliere et al. [33]. The joint exhibits a continuous flow of plasticised material between AS and RS. Under all welding conditions joints free of volume defects such as tunnels, and pinholes were formed with complete penetration. This indicates that the generated frictional heat, stirring action, and material plastic deformation are sufficient for
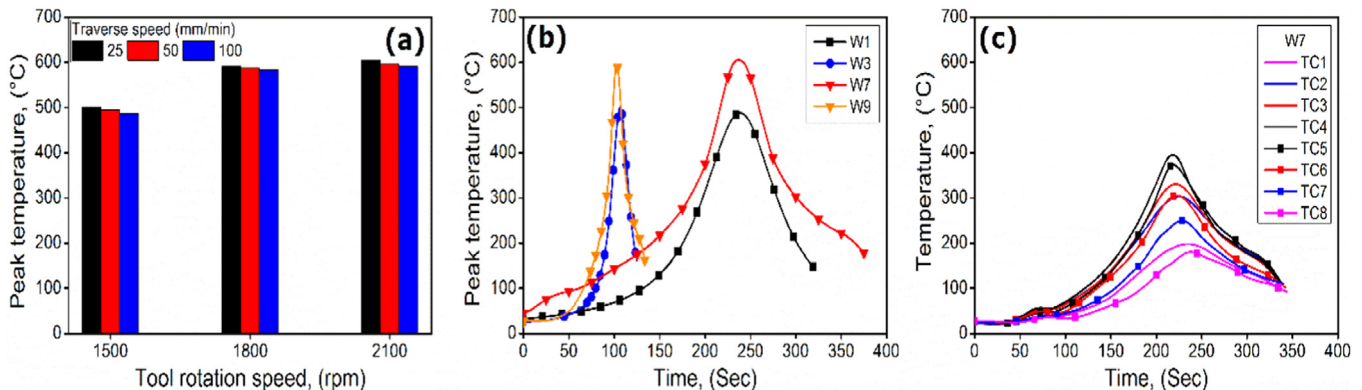

Fig. 2. (a) Maximum generated temperature in the NZ, (b) effect of FSW parameters on thermal history in the NZ, and (c) typical thermal history on the advancing and retreating side of W7.
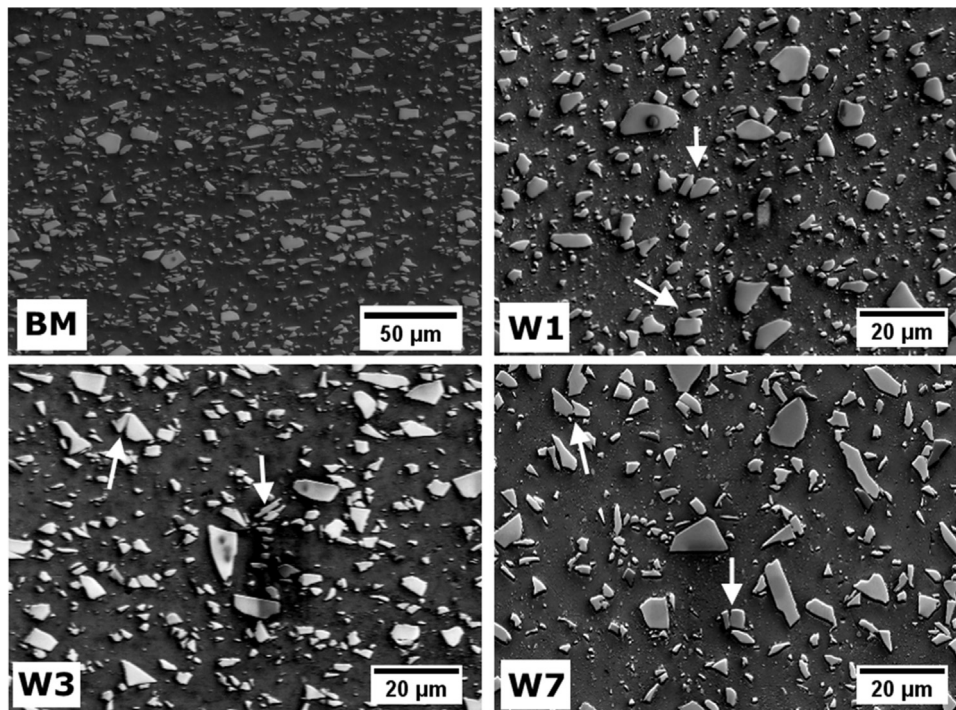
Fig. 4. SEM micrographs of BM and typical FSW joints under different welding conditions. Note difference in scales.

complete plasticization and material flow for proper coalescence [11]. However, joint W8 contained a macro defect under the top surface (Fig. 3(d)), which is considered to be related to the fretting damage of the nitride layer.

To evaluate the effects of both of the tool rotation and traverse speeds on the distribution of SiC particles in the matrix alloy, as well as matrix grain structure, the SEM and EBSD results of the BM and typical FSW joints (W1, W3, and W7) are presented in Figs. 4 and 5, respectively. As shown in Fig. 4, the microstructure of the BM shows a reasonable distribution of the reinforcement particles in the matrix alloy having an average size of around 6 μm and an average volume fraction of 17.5%. On the other hand, the SEM micrographs of W1, W3 and W7 FSW joints show a fairly homogeneous distribution of SiC in the NZ as a result of severe plastic strain caused by the rotating tool [11]. More homogeneity was achieved at lower welding traverse speed (W1). It was also observed that the SiC particles were fractured in the NZ (white arrow) and the edges of the particles were blunted compared to the sharp SiC particles in the BM. This leads to refinement of SiC with an average size of around 1, 3, and 1.7 μm in W1, W3, and W7, respectively, with the presence of small rounded particles, which did not appear in BM. This phenomenon can be related to the abrasion and stirring action between the reinforcement particles and tool pin circumference, as well as to the extremely high plastic deformation occurred during FSW [9]. As a result of particle refinement, the average volume fraction of SiC in the matrix alloy increases to around 22%, 19%, and 21% in W1, W3, and W7, respectively.

Fig. 5(a) shows the related EBSD Euler orientation and grain boundary maps (BM, W1, W3 and W7). It should be mentioned that for the cross-weld samples the locations of data acquisitions for EBSD analysis were focused on the centre of the NZ, to avoid the effect of complicated material flow in the top and bottom parts in this zone [34]. In these maps, individual grains were coloured according to their crystallographic orientations relative to the welding direction, and the black and red lines represent the HAGBs and LAGBs, where the white area represents the SiC. In terms of morphology, it can be seen that the evolved grain structures under different welding conditions were broadly similar to each other. In all cases, the grains were often not

entirely delineated by a continuous HAGBs perimeter, and therefore the microstructure was represented in term of grain size and misorientation angles (a mixture of LAGBs and HAGBs) as shown in Fig. 5((b) and (c)). The grain size was measured based on either the area-weighted mean size D^A or the arithmetical mean size D^N [35]. BM microstructure shows a significant variation in the grain size ranging from 3 to 39 μm having a mean diameter of around 13 μm, with a mixture of HAGBs (high surface energy) and a high fraction of low energy substructure network LAGBs (subgrains). This can be related to the fact that when the polycrystalline metal deformed a large number of LAGBs are formed, as the LAGBs consist of arrays of edge dislocations and its structure and properties depend on the misorientation [36].

In comparison with BM, more homogeneous microstructures with fine equiaxed grains were formed in the NZ. At the lowest tool rotation speed of 1500 rpm, extra fine equiaxed grains having a size of around 2 μm were formed in the NZ combined by a low fraction of LAGBs (Fig. 5-W1). Grain growth to about 8 μm happened with the increase of tool rotation speed to 2100 rpm (Fig. 5-W7), as a result of high welding temperature, which is in agreement with a study conducted by Lee et al. [37]. In both cases, the grain boundaries are highly dominated by HAGBs. Consequently, the LAGBs increases with the increase in traverse speed, while the local misorientation change in a few grains, and it is more evident with 1500 rpm rotational speed (Fig. 5-W3). From the analysis of the misorientation angle distribution in Fig. 5(c), five important observations can be made: (i) The BM consists of HAGBs and a high fraction of LAGBs. (ii) The fraction of HAGBs increases under all welding conditions in comparison to BM. (iii) For all examined cases, at a low angle, the misorientation distribution is characterised by a sharp angle peak whereas a broader peak was observed in the angular range of 5–60°. (iv) The HAGBs are close to the random distribution under most welding conditions. (v) The formation of LAGBs is more affected by traverse speed than rotation speed.

3.3. Mechanical characterisation

3.3.1. Microhardness distribution

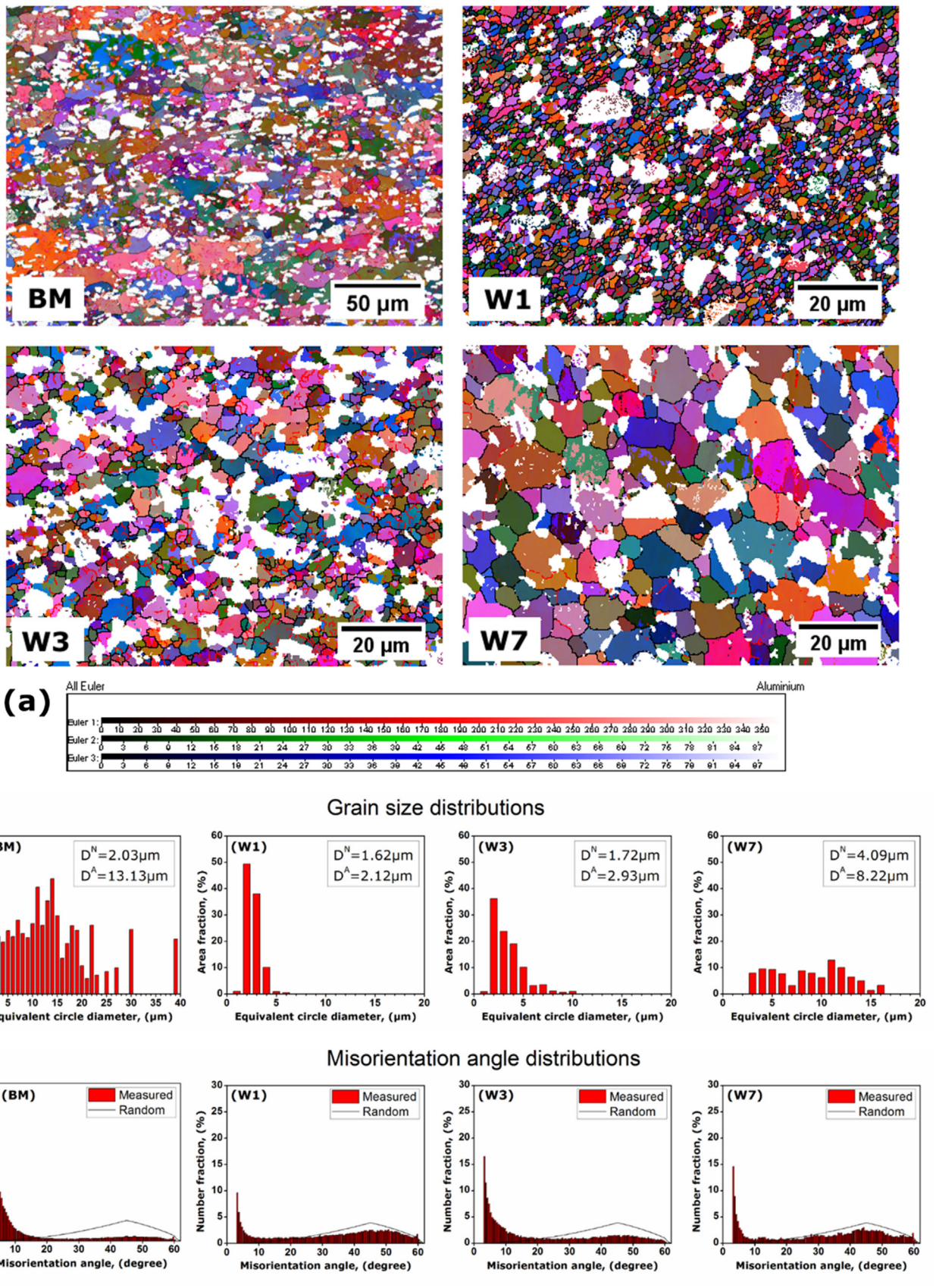Fig. 6(a) and (b) presents the distributions of hardness along the

Fig. 5. EBSD results of BM and typical FSW joints under different welding conditions, (a) grain morphology and the distribution of HAGBs (black line), and LAGBs (red line), (b) grain size distribution, and (c) misorientation angle distribution. Note difference in scales (For interpretation of the references to color in this figure legend, the reader is referred to the web version of this article.).
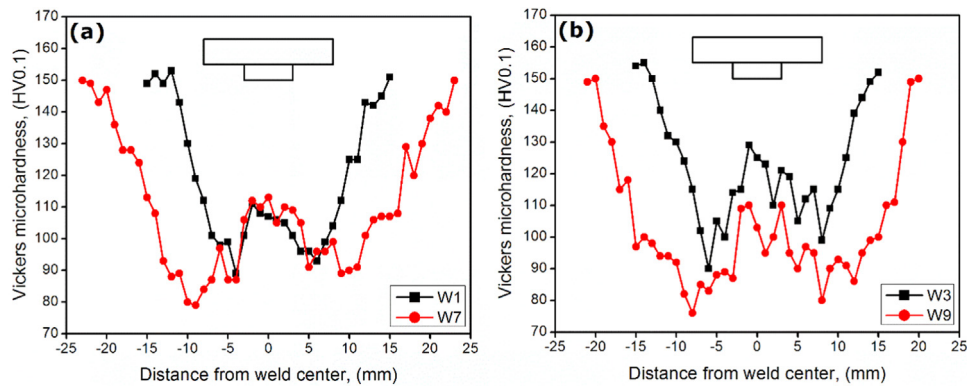
Fig. 6. Microhardness profiles along the cross-weld at different traverse speed; (a) 25 mm/min, (b) 100 mm/min.

mid-thickness of the cross-weld joints welded at 1500, and 2100 rpm with traverse speed of 25 and 100 mm/min (corners of welding matrix). The hardness profile exhibit asymmetric distribution with a typical "W" shape for all joints, similar to that seen in AA2009/SiC (AMC) FSW joints [38]. Regardless of the welding parameters, a softening process occurred in the FSZ, and the hardness value of the BM was much higher than that of the FSZ of around 150 HV. For the joints fabricated at the lowest traverse speed of 25 mm/min, a wider TMAZ and HAZ were formed with the increase of tool rotation speed from 1500 to 2100 rpm (Fig. 6(a)), associated with a higher peak temperature and exposure time. However, the hardness value in the NZ was nearly the same in the ranging from 95 to 110 HV. AS the traverse speed increased to 100 mm/min (Fig. 6(b)), the average hardness of the NZ increased by about 20 HV combined by a reduction in the TMAZ and HAZ. Furthermore, the width of the high hardness zone in the joints fabricated at a traverse speed of 100 mm/min was larger than that of the joints welded at 25 mm/min. It is believed that this variation in the hardness of FSZ is a result of the difference of microstructures characterisations, which are controlled by welding parameters [37].

3.3.2. Monotonic tensile properties

Fig. 7(a) shows the stress-strain curves of the BM, cross-weld (W1-W9), and longitudinal weld (WL3). Their ultimate tensile strength

(UTS), yielding stress (YS), and percentage of elongation (% El) are compared in the bar graph (Fig. 7(b)). Note that the cross-weld sample microstructure is heterogeneous as it is consist of four zones, i.e., BM, HAZ, TMAZ and NZ (Fig. 3(c)). Meanwhile, the longitudinal specimen contains only uniform fine equiaxed grains from the NZ. According to the stress-strain curves, the as-received AMC shows a tensile strength of about 419 MPa with a total elongation to failure of around 2.8%. In contrast, the cross-weld samples exhibit a higher ductility with a drop in the tensile strength as compared with BM. The reduction in tensile strength of AMC (AA6061/Al$_2$O$_3$) FSW joints was also reported by Cavaliere et al. [18]. Furthermore, the stress-strain curve related to BM shows continuous yielding, while most of the welded samples exhibit a distinct yielding serration "jerky flow" phenomenon and similar findings have been reported by Mahmoudiniya et al. [39] and Pathak et al. [40]. Judging from Fig. 7(b), the mechanical properties of FSW joints are affected significantly by the welding parameters. It is shown that the joint fabricated at lowest heat input (W3) showing a higher strength (joint efficiency reaches about 75%) with the adequate elongation of around 5%. On the other hand, the joint welded at highest heat input and lower cooling rate (W7) shows a lowest joint strength (joint efficiency of about 52%) with a severe drop in the elongation. Surprisingly, the longitudinal welded samples (WL3) shows smooth curve characterised by a moderate combination between strength and elongation
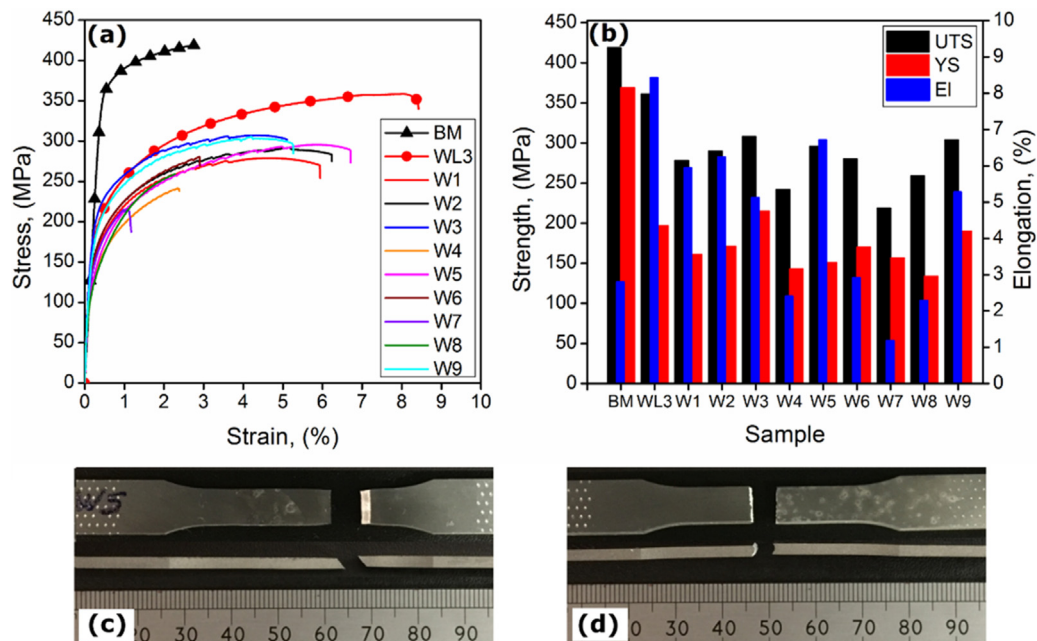

Fig. 7. Tensile properties of BM, cross-weld (W1-W9), and longitudinal weld (WL3); (a) stress-strain curves, (b) bar graphs representing strength and % of elongation, and (c, and d) fracture locations.
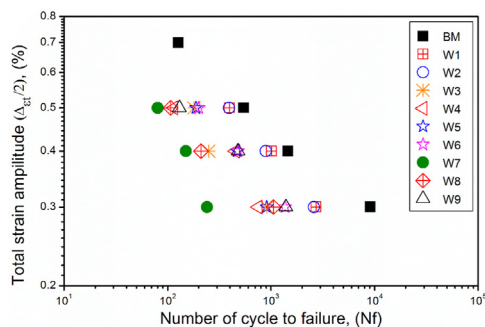
Fig. 8. Total strain amplitudes versus the number of cycles to failure for the BM and FSW joints.

of about 361 MPa (86% joint efficiency), and 8.5% (67% increase in elongation) than the BM, respectively. This can be related to the homogeneous fine grain structure in the entire sample. The location of the fracture in the typically tested samples is shown in Fig. 7((c), and (d)). Under most welding conditions, the FSW joints exhibited shear fracture mode occurred in the HAZ (AS) (see Fig. 7(c)) oriented at an angle of about 45°, as also presented by Moreira et al. [41], because of the loss of strength in this area as observed in the microhardness measurements. However, in W8 FSW joints fracture occurred in the stirring zone (see Fig. 7(d)), which can be related to macro defects on the top surface of the joint (Fig. 3(d)).

3.3.3. Low cycle fatigue life and cyclic deformation behaviour

The total strain amplitudes ($\Delta_{\varepsilon t}/2$) as a function of the fatigue life (i.e., the number of cycle to failure, Nf) of the BM and FSW joints is plotted in Fig. 8. As it is evident, for a given total strain, the fatigue life of the FSW samples is lower than that of the BM. However, the results witnessed that, at high strain amplitude, the fatigue life show an apparent convergence in the BM and the welded joints. A similar trend has been also reported by Ceschini et al. [24] in FSW of AA6061 composite renforced with Al_2O_3. This behaviour can be attributed to the lower ductility of the composite metal. At high plastic strains amplitude, the cyclic ductility of the material limits the amount of induced plastic strain, and thus, the number of cycles that can be generated before fracture. The reduction in the fatigue life was more evident on the joints fabricated by using tool rotation speed of 1800 and 2100 rpm. On the other hand, significant enhancements of LCF property are achieved in the W1, and W2 even so at high strain amplitude (0.5%). This distinctive LCF performance is due to the fact that the formation of very fine equiaxed grains dominated by HAGBs in the NZ (see Fig. 5) combined with a high fraction of ultra-fine reinforcement particles can restrict the movement of dislocations most effectively [42].

Fig. 9((a) and (b)) illustrates the typical nominal stress-total strain hysteresis loops of the first and mid-life cycles at a given strain amplitude of 0.3% and 0.5% for the BM and W1. For the BM sample, the hysteresis loop area was nearly constant during the specimen life. Meanwhile, there is a significant change in the loop area in the case of FSW joints. These results are similar to those of FSW of $AA7005/Al_2O_3$ [43]. By comparison of these figures, several features can be pointed out: i) For a given total strain, the amount of plastic strain is much higher for the FSW joints than for the BM, and this is in agreement with its lower fatigue life. ii) The evolution of the stress with the number of cycles in the BM was found to rise slightly, while in FSW joints, the cyclic hardening was more evident regardless of strain amplitudes. iii) Both of the BM and FSW joints exhibited nearly symmetrical hysteresis loops at both the outset and mid-life, representing an isotropic cyclic
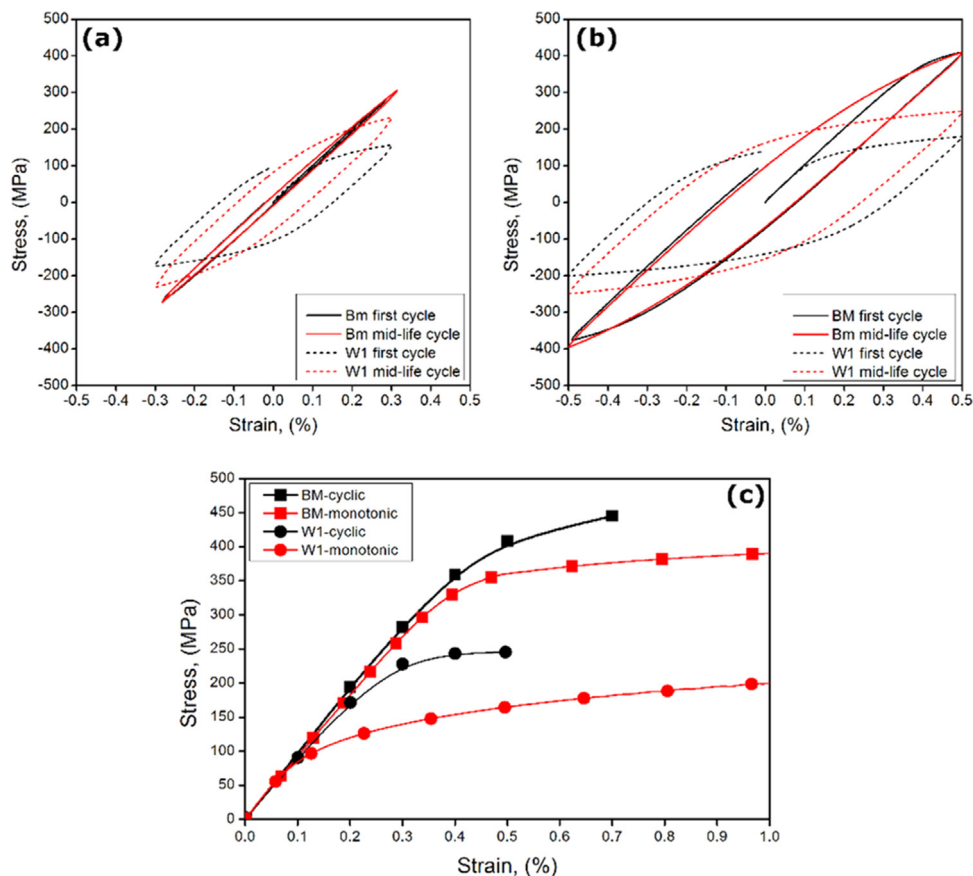

Fig. 9. Hysteresis loops for the BM and typical FSW joints (W1) at different strain amplitudes, (a) 0.3%, (b) 0.5%; (c) comparison of cyclic and monotonic stress-strain curves for BM, and W1.

hardening response. The extent of cyclic hardening is revealed by cyclic stress-strain curves and can be compared to the monotonic curves. Two approaches for generating cyclic stress-strain curves have been employed in this work. Saturated hysteresis loops and half of fatigue life cycle are used for the BM and FSW joints, respectively [44]. Fig. 9(c) compares the cyclic and monotonic stress-strain responses of the BM and typical FSW joint (W1). For both of them, it can be seen that the cyclic stress-strain curve lies above the monotonic stress-strain curve, indicating cyclic hardening behaviour.

4. Discussion

4.1. Heat generation and microstructure evolution during FSW

Except for the plunging and retracting tool steps, heat is generated at a constant rate during the intermediate period, and similar geometry, structure and properties are formed in the cross-welds, which indicates a quasi-steady behaviour [45]. According to the concept of a pseudo heat index (ω^2/V), the heat generation in FSW is governed by two significant factors, i.e. the tool rotation and traverse speeds. The combined effect of these two factors is defined as the weld pitch (ratio of traverse speed to the rotational speed (mm/rev)), which is to control the energy generated per unit length [46]. Fig. 10(a) shows the effect of weld pitch on the maximum generated temperature in the NZ, indicates two tendencies for attention. Firstly, for joints welded with the same traverse speed, the reduction in peak temperature as a function of weld pitch was so sharp. For example, the increase of weld pitch by decreasing the tool rotation speed from 2100 to 1500 rpm (29%) caused the peak temperature to decrease by about 17%. Secondly, for joints welded with a similar rotational speed, a lower sharpness in the drop of welding temperature has obtained. The rises of traverse speed from 25 to 100 mm/min (300%) increases the weld pitch, lead to a reduction of the peak temperature by nearly 2.5,1.2% and 1.5% for tool rotation speed of 1500, 1800 and 2100 rpm, respectively. These findings are in agreement with the finding of Seidel and Reynolds [47]. They reported that the amount of energy input (Joules/meter) relates to the specific weld pitch, as it is increase, a reduction in the energy per unit length of weld occurred.

The observed microstructural difference between the BM and FSW joints are believed to be related to the temperature gradient, which is controlled by welding parameters [48,49]. Fig. 10(b) displays the relationship between the peak temperature and the mean grain size in the NZ. According to the figure, two behaviours are observed. Firstly, at the lowest tool rotation speed (1500 rpm), larger grains were formed by increasing the traverse speed (W3 > W2 > W1). This behaviour can be related to the incomplete recrystallisation in the NZ, as a result of lower heat input, insufficient plastic deformation, and high cooling rate, which is confirmed by the formation of low fraction of HAGBs (see Fig. 5-W3). Also, as the traverse speed decreases, the volume fraction of

reinforcement particles increases due to SiC refinement (Fig. 4), therefore, the microstructure refinement is also attributed to grain boundary pinning with reinforcement particles [50]. Secondly, the results indicate structural coarsening by increasing rotational speed under the studied conditions, and this effect was found to be more pronounced at the highest rotation speed of 2100 rpm. In agreement with previous studies [12,34], the microstructure is coarsened with the increasing of welding temperature. On the other hand, finer recrystallised grain in the NZ was found accompanying the increase of the traverse speed, due to low exposure time at high temperature and high cooling rate as reported by Murugan and Kumar [17].

As a result, under all welding conditions, the grain structure in the NZ is characterised by smaller grain size and a higher fraction of HAGBs in comparison with BM due to continuous dynamic recrystallisation (CDR). However, the grain structure is different due to the complex interaction between the generated temperature and material flow during FSW. The mechanism of microstructure evolution continuously and uniformly dominated by HAGBs in the NZ can be explained by the hot working process under large strain deformation conditions. Firstly, a large number of dislocations were introduced in the stirring zone when the material deformed extensively and extruded through the confined area between the pin and the cold material. The dislocation climb, cross-slip, and glide occur quickly and extensively at high temperatures in metals of high stacking fault energy (SFE) such as aluminium (around 170 mJ m^{-2}), which is the mechanism of dynamic recovery (DR), and results in the formation of more organised dislocations arrangement (LAGBs) (subgrain). The subgrain size can be related to Zenner-Hollomon parameter (Z), as the material plastic flow at an elevated temperature where the deformation and softening processes occur depends on the deformation temperature, strain rate, and strain [51]. Recently, Mahmoudiniya et al. [39] reported an empirical equation for predicting the final grain size of FSW DP700 steel based on the Z parameter. They mention that the increase in temperature decreases the Z parameter and increases the recrystallised grain size. This gives an explanation to the coarsening of the microstructure with increasing rotational speed because the Z parameter experienced a decreasing trend with increasing rotational speed (higher welding temperature). Secondly, the CDR process occurs as the increasing of applied strain resulting in introduced dislocations continuously to the subgrains by further deformation. As the subgrain size is almost independent of the strain during deformation at high temperature, instead the subgrains rotate as they accommodate more dislocations into their boundaries, forming equiaxed grains having a size comparable to the subgrain with HAGBs [52–54]. This gives an explanation to the dominating of HAGBs on the microstructure of the NZ. Both of the DR and CDR processes are essential in FSW, as they lower the flow stress of the material, so enabling it to be deformed more efficiently.
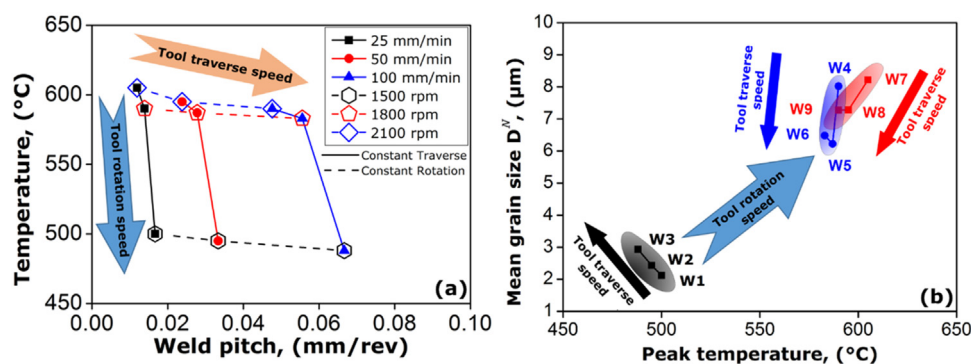

Fig. 10. (a) Relationship between peak temperatures and weld pitch at constant tool rotation and traverse speed, (b) relationship between mean grains sizes and peak temperature.

4.2. Hardness profile of friction stir welded AA6092/SiC

The effect of FSW parameters on the hardness profile of AMCs joints displayed in Fig. 6. According to the figure, the hardness profile of the FSZ is dependent on the process parameters, and the measured hardness value is lower than the BM. As reported in the other studies, the reduction in hardness is usual in heat-treatable artificially aged aluminium alloy (6xxx-T6 series) [28,54,55]. Microstructural evolution due to thermomechanical effect during FSW, in term of strengthening precipitate, and grain size can be considered as two mechanisms for softening in FSW joints. The hardness value decreases in the HAZ, although there is no apparent difference in the microstructure from that of the BM, indicating that the thermally induced cycle during FSW has a significant influence on this zone. Also, the hardness reaches a minimum in the TMAZ region, as it is exposed to the grain deformation and thermal cycle. As there is no change in the size or shape of reinforcement particles in the HAZ and TMAZ, the softening process can be attributed to the annealing or overaging of strengthening precipitate. According to Gatea et al. [56], the hardness of AA 6092/SiC/17.5p dropped when heat treated to 415 °C (O-condition) as compare to T6-condition, which was nearly the same as the temperature in the HAZ and TMAZ of FSW joints. They claim this is due to the reduction of Si concentration in the matrix/particle interface and dissolution of Al_2Cu (orthorhombic crystal structure) and reprecipitated $Al_4Cu_2Mg_8Si_7$ (hexagonal crystal structure). Also, Olea et al. [57] claim the reduction in the hardness of the TMAZ to the overaging of strengthening precipitate, as transformed from needles to lath morphology.

The most significant recovery in hardness is observed in the NZ, which can be attributed to the refinement of both the matrix grain and SiC particles and the generation of dislocations at the matrix-SiC interface due to high differences in the thermal expansion coefficient between SiC and aluminium matrix [9,16]. Furthermore, the NZ experiences the highest temperatures generated by the welding process (above the solvus of the initial precipitate of around 540 °C), leading to the dissolution of precipitates and the formation of a supersaturated solid solution (SSSS). The SSSS undergos expected natural ageing and hence increases the hardness [58].

4.3. Structural property in the friction stir welded AA6092/SiC

Fig. 11 presents the relationship between the tensile strength, fatigue life and mean grain size. According to Fig. 11(a), two opposite tendencies can be observed relating the effect of grain size on the tensile strength. Firstly, at the lowest tool rotation speed of 1500 rpm, the tensile strength of FSW joints is improved with an increase of mean grain size (W3 > W2 > W1). The increase in monotonic strength of FSW joints can be attributed to several mechanisms. Chawla et al. [5] proved that the strengthening of AMC is significantly affected by the microstructure of the aluminium matrix and reinforcement particles. For the studied BM in T6 metallurgical conditions (strengthened by

strengthening precipitates), a higher traverse speed results in insufficient stirring time for complete recrystallisation (producing a coarse grain structure). This, combined with the partial dissolution of the precipitates resulting from the FSW thermal cycles and subsequent re-precipitation during natural ageing after FSW, results in an increase in strength [32].

Furthermore, according to the Taylor strengthening mechanism, volumetric strain occurs in the composite when using a fast cooling rate due to the thermal mismatch between the aluminium matrix and SiC particles which leads to the generation of geometrically necessary dislocations (GNDs) around the reinforcement particles. As the interaction of the mobile dislocations increases, flow stress of composite metal increase [59,60]. This mechanism is confirmed by the formation of a high fraction of LAGBs substructure at higher traverse speed (Fig. 5-W3).

Secondly, at higher tool rotation speed (1800 and 2100 rpm) the tensile strength of weldments goes through a maximum with a higher traverse speed as a result of the evolution of entirely recrystallised finer grain. This is in agreement with the Hall-Petch strengthening mechanism, as grain refinement and the formation of a high fraction of HAGBs leads to the increase of the resistance to the motion of dislocation and pile-up of dislocations at grain boundaries, which plays a significant role in enhancing resistance to plastic flow [61]. The effect of grain boundary on the strength of metal is also confirmed in Al–7% Si cast alloy and SAE 1020 steel [36,62].

The fatigue properties are frequently correlated with tensile properties [36]. In LCF the strain resistance depends on the ductility of the metal, i.e. higher ductility higher the fatigue life. Although the tensile characterisation of the welded joints showed higher ductility than the BM, the fatigue life of FSW joints is lower than the BM and vary based on the welding conditions (see Fig. 8). The variation in fatigue behaviour is mainly dependent on the evolved microstructure characterisation and cyclic strain range [63,64]. Fig. 11(b) displays the relationship between the fatigue life and grain size at different strain amplitude. As shown in the figure, two opposite tendencies are pointed; firstly, at lowest tool rotation speed (1500 rpm), the increase of traverse speed leads to lower fatigue life (W1 > W2 > W3) under all strain amplitudes, this trend is opposite to that of tensile behaviour (Fig. 11(a)). Secondly, at high tool rotation speeds of 1800 and 2100 rpm, faster traverse speed improves the fatigue life of FSW weldment, i.e. W9 > W8 > W7.

For both trends, it can be seen that the fatigue life has been improved with the formation of smaller grain size combined with the high fraction of HAGBs (see Fig. 5), and high volume fraction of SiC. The formation of HAGBs almost leads to high ductility, and as the diameter of the grain is reduced more of the grain boundaries properties will be reflected in the centre of the grain. Therefore, this can effectively prevent macroscopic plastic deformation, and minimise microscopic localised plastic strain under specific cyclic stress amplitude. Also, in AMC, an increase in the volume fraction of the hard ceramic reinforcing
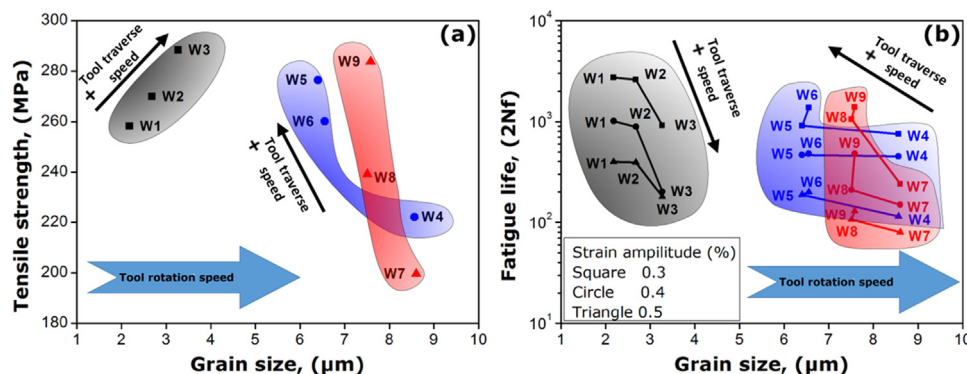

Fig. 11. Mechanical properties versus mean grain size; (a) tensile strength; (b) fatigue life.

particulates (due to the particle refinement) increases dislocation density and reduces grain size. These microstructural changes tend to increase the resistance offered to the motion of mobile dislocations. Furthermore, load transfer from the matrix to the reinforcement is a significant contributor to composite strengthening [59,65].

The cyclic hardening behaviour of the BM and FSW joints during fully reversed cyclic straining under all strain amplitude (Fig. 9) could be attributed to the following reasons; (i) The competing and synergistic effects of stress (load) transfer between the soft and ductile aluminium alloy matrix and the hard and brittle ceramic reinforcement particle (SiC) [66]. (ii) Grain refinement, as the grain boundaries act as barriers to dislocations movement, thus the strain hardening in the smaller grain size is higher than the coarse grains [67]. (iii) The pre-existence of high dislocation density in the aluminium matrix produced by the presence of the SiC reinforcement due to a mismatch in the coefficients of thermal expansion [68,69]. (iv) An increase in the storage dislocation density during cyclic plastic deformation, as they accumulate by randomly trapping each other, which is associated with plastic strain, or they are required for compatible deformation of various parts of the crystal (GNDs) associated with plastic strain gradient [64].

5. Conclusions

In the current work, the effect of FSW parameters (tool rotation and traverse speed) on the heat generation and microstructure evolution of AA6092/SiC/17.5p-T6 joints and its effect on the tensile and LCF properties are systematically examined. The rotational speed has a more significant effect on the generated peak temperature, while the traverse speed controls the exposure time and subsequent cooling rate. The microstructure of NZ exhibits an elliptical shape, and fine equiaxed grains resulted from the CDR process. Grain growth in the NZ occurs as a result of incomplete CDR or in particular when exposure time at high temperature is very long. The grain boundary in the NZ is a mixture of LAGBs and HAGBs, and it is fraction controlled by the traverse speed. The SEM micrographs reveal a homogeneous distribution of reinforcement particles (SiC) in the NZ with an increase in the volume fraction because of particles refinement. The microhardness distribution of the welded joints under different welding conditions exhibited typical "W" shape features. The width of the minimum hardness zone varied with the induced temperature and corresponded accordingly with the range of the HAZ and TMAZ. The tensile properties of the joint welded at a rotational speed of 1500 rpm and traverse speed of 100 mm/min are the best amongst all weld joints tested. The joint efficiency of the welded joint reached 75% of the BM, while the elongation increases by 44%. Increases in LCF life of the AA6092/SiC/17.5p FSW joints were observed with decreased grain and reinforcement particle size and increased particle volume fraction. FSW parameters control these microstructural features, and it is found that the combination of tool rotation speed of 1500 rpm with a traverse speed of 25, and 50 mm/min resulted in optimal joints performance. The cyclic stress-strain curves of the FSW composite showed evidence of progressive isotropic hardening to failure for all cyclic strain amplitudes, while the BM showed less hardening ability.

Acknowledgements

Data availability

The raw/processed data required to reproduce these findings cannot be shared at this time due to technical or time limitations.

References

[1] T. Prater, Friction stir welding of metal matrix composites for use in aerospace structures, Acta Astronaut. 93 (2014) 366–373.

[2] A.K. Kaw, Mechanics of Composite Materials, CRC press, 2005.

[3] M. Levin, B. Karlsson, Crack initiation and growth during low-cycle fatigue of discontinuously reinforced metal-matrix composites, Int. J. Fatigue 15 (5) (1993) 377–387.

[4] J.E. Allison, J.W. Jones, Fatigue behavior of discontinuously reinforced metal-matrix composites, in: S. Suresh, A. Mortensen, A. Needleman (Eds.), Fundamentals of Metal-Matrix Composites, Elsevier, 2013.

[5] N. Chawla, U. Habel, Y.-L. Shen, C. Andres, J. Jones, J. Allison, The effect of matrix microstructure on the tensile and fatigue behavior of SiC particle-reinforced 2080 Al matrix composites, Metall. Mater. Trans. A 31 (2) (2000) 531–540.

[6] D. Storjohann, O.M. Barabash, S.S. Babu, S.A. David, P.S. Sklad, E.E. Bloom, Fusion and friction stir welding of aluminum metal-matrix composites, Metall. Mater. Trans. A 36A (2005) 3237–3247.

[7] O.S. Salih, H. Ou, W. Sun, D. McCartney, A review of friction stir welding of aluminium matrix composites, Mater. Des. 86 (2015) 61–71.

[8] D.R. Ni, D.L. Chen, D. Wang, B.L. Xiao, Z.Y. Ma, Tensile properties and strain-hardening behaviour of friction stir welded SiCp/AA2009 composite joints, Mater. Sci. Eng.: A 608 (2014) 1–10.

[9] Y. Bozkurt, H. Uzun, S. Salman, Microstructure and mechanical properties of friction stir welded particulate reinforced AA2124/SiC/25p-T4 composite, J. Compos. Mater. 45 (21) (2011) 2237–2245.

[10] H. Nami, H. Adgi, M. Sharifitabar, H. Shamabadi, Microstructure and mechanical properties of friction stir welded Al/Mg2Si metal matrix cast composite, Mater. Des. 32 (2) (2011) 976–983.

[11] K. Kalaiselvan, I. Dinaharan, N. Murugan, Characterization of friction stir welded boron carbide particulate reinforced AA6061 aluminum alloy stir cast composite, Mater. Des. 55 (2014) 176–182.

[12] P. Periyasamy, B. Mohan, V. Balasubramanian, Effect of heat input on mechanical and metallurgical properties of friction stir welded AA6061-10% SiCp MMCs, J. Mater. Eng. Perform. 21 (11) (2012) 2417–2428.

[13] P. Periyasamy, B. Mohan, V. Balasubramanian, S. Rajakumar, S. Venugopal, Multi-objective optimization of friction stir welding parameters using desirability approach to join Al/SiCp metal matrix composites, Trans. Nonferr. Met. Soc. China 23 (4) (2013) 942–955.

[14] K. Kalaiselvan, N. Murugan, Role of friction stir welding parameters on tensile strength of AA6061–B4C composite joints, Trans. Nonferr. Met. Soc. China 23 (3) (2013) 616–624.

[15] I. Dinaharan, N. Murugan, Effect of friction stir welding on microstructure, mechanical and wear properties of AA6061/ZrB2 in situ cast composites, Mater. Sci. Eng.: A 543 (2012) 257–266.

[16] I. Dinaharan, N. Murugan, Optimization of friction stir welding process to maximize tensile strength of AA6061/ZrB2 in-situ composite butt joints, Met. Mater. Int. 18 (1) (2012) 135–142.

[17] N. Murugan, B. Ashok Kumar, Prediction of tensile strength of friction stir welded stir cast AA6061-T6/AlNp composite, Mater. Des. 51 (2013) 998–1007.

[18] P. Cavaliere, E. Cerri, L. Marzoli, J. Dos Santos, Friction stir welding of ceramic particle reinforced aluminium based metal matrix composites, Appl. Compos. Mater. 11 (2004) 247–258.

[19] L.M. Marzoli, Av Strombeck, J.F. Dos Santos, C. Gambaro, L.M. Volpone, Friction stir welding of an AA6061/Al2O3/20p reinforced alloy, Compos. Sci. Technol. 66 (2) (2006) 363–371.

[20] X.G. Chen, M. da Silva, P. Gougeon, L. St-Georges, Microstructure and mechanical properties of friction stir welded AA6063–B4C metal matrix composites, Mater. Sci. Eng.: A 518 (1–2) (2009) 174–184.

[21] B. Ashok Kumar, N. Murugan, Optimization of friction stir welding process parameters to maximize tensile strength of stir cast AA6061-T6/AlNp composite, Mater. Des. 57 (2014) 383–393.

[22] G. Minak, L. Ceschini, I. Boromei, M. Ponte, Fatigue properties of friction stir welded particulate reinforced aluminium matrix composites, Int. J. Fatigue 32 (1) (2010) 218–226.

[23] A. Pirondi, L. Collini, D. Fersini, Fracture and fatigue crack growth behaviour of PMMC friction stir welded butt joints, Eng. Fract. Mech. 75 (15) (2008) 4333–4342.

[24] L. Ceschini, I. Boromei, G. Minak, A. Morri, F. Tarterini, Microstructure, tensile and fatigue properties of AA6061/20 vol% Al2O3 friction stir welded joints, Compos. Part A: Appl. Sci. Manuf. 38 (4) (2007) 1200–1210.

[25] Z. Ma, A. Feng, D. Chen, J. Shen, Recent advances in friction stir welding/processing of aluminum alloys: microstructural evolution and mechanical properties, Crit. Rev. Solid State Mater. Sci. 43 (4) (2018) 269–333.

[26] J. Polak, Cyclic Plasticity and Low Cycle Fatigue Life of Metals, , Elsevier Science Publishers Amsterdam, The Netherlands, 1991.

[27] Y.S. Sato, M. Urata, H. Kokawa, Parameters controlling microstructure and hardness during friction-stir welding of precipitation-hardenable aluminum alloy 6063, Metall. Mater. Trans. A 33 (3) (2002) 625–635.

[28] R.S. Mishra, Z.Y. Ma, Friction stir welding and processing, Mater. Sci. Eng.: R: Rep. 50 (1–2) (2005) 1–78.

[29] R. Nandan, T. DebRoy, H. Bhadeshia, Recent advances in friction-stir welding–-process, weldment structure and properties, Prog. Mater. Sci. 53 (6) (2008) 980–1023.

[30] J.A. Schneider, Temperature distribution and resulting metal flow, in: R.S. Mishra, M.W. Mahoney (Eds.), Friction Stir Welding and Processing, ASM International, 2007.

[31] F. Cioffi, R. Fernández, D. Gesto, P. Rey, D. Verdera, G. González-Doncel, Friction stir welding of thick plates of aluminum alloy matrix composite with a high volume fraction of ceramic reinforcement, Compos. Part A: Appl. Sci. Manuf. 54 (2013) 117–123.

[32] A. Feng, B. Xiao, Z. Ma, Effect of microstructural evolution on mechanical properties of friction stir welded AA2009/SiCp composite, Compos. Sci. Technol. 68 (9) (2008) 2141–2148.

[33] P. Cavaliere, G. Rossi, R. Di Sante, M. Moretti, Thermoelasticity for the evaluation of fatigue behavior of 7005/Al2O3/10p metal matrix composite sheets joined by FSW, Int. J. Fatigue 30 (1) (2008) 198–206.

[34] S. Mironov, T. Onuma, Y. Sato, H. Kokawa, Microstructure evolution during friction-stir welding of AZ31 magnesium alloy, Acta Mater. 100 (2015) 301–312.

[35] B. Mouawad, X. Boulnat, D. Fabrègue, M. Perez, Y. De Carlan, Tailoring the microstructure and the mechanical properties of ultrafine grained high strength ferritic steels by powder metallurgy, J. Nucl. Mater. 465 (2015) 54–62.

[36] G. Dieter, Mechanical Metallurgy McGraw-Hill Book Company (UK) Limited, ISBN-0-07-084187-x1988.

[37] W. Lee, Y. Yeon, S. Jung, Joint properties of friction stir welded AZ31B–H24 magnesium alloy, Mater. Sci. Technol. 19 (6) (2003) 785–790.

[38] D. Wang, Q.Z. Wang, B.L. Xiao, Z.Y. Ma, Achieving friction stir welded SiCp/Al–Cu–Mg composite joint of nearly equal strength to base material at high welding speed, Mater. Sci. Eng.: A 589 (2014) 271–274.

[39] M. Mahmoudiniya, A.H. Kokabi, S. Kheirandish, L.A. Kestens, Microstructure and mechanical properties of friction stir welded ferrite-martensite DP700 steel, Mater. Sci. Eng.: A (2018).

[40] N. Pathak, K. Bandyopadhyay, M. Sarangi, S.K. Panda, Microstructure and mechanical performance of friction stir spot-welded aluminum-5754 sheets, J. Mater. Eng. Perform. 22 (1) (2013) 131–144.

[41] P.M.G.P. Moreira, A.M.P. de Jesus, A.S. Ribeiro, P.M.S.T. de Castro, Fatigue crack growth in friction stir welds of 6082-T6 and 6061-T6 aluminium alloys: a comparison, Theor. Appl. Fract. Mech. 50 (2) (2008) 81–91.

[42] J.N. Hall, J.W. Jones, A.K. Sachdev, Particle size, volume fraction and matrix strength effects on fatigue behavior and particle fracture in 2124 aluminum-SiCp composites, Mater. Sci. Eng.: A 183 (1–2) (1994) 69–80.

[43] L. Ceschini, I. Boromei, G. Minak, A. Morrri, F. Tarterini, Effect of friction stir welding on microstructure, tensile and fatigue properties of the AA7005/10 vol% Al2O3p composite, Compos. Sci. Technol. 67 (3_4) (2007) 605–615.

[44] S.K. Paul, N. Stanford, A. Taylor, T. Hilditch, The effect of low cycle fatigue, ratcheting and mean stress relaxation on stress–strain response and microstructural development in a dual phase steel, Int. J. Fatigue 80 (2015) 341–348.

[45] R. Nandan, G. Roy, T. Lienert, T. Debroy, Three-dimensional heat and material flow during friction stir welding of mild steel, Acta Mater. 55 (3) (2007) 883–895.

[46] S. Chowdhury, D. Chen, S. Bhole, X. Cao, Tensile properties of a friction stir welded magnesium alloy: effect of pin tool thread orientation and weld pitch, Mater. Sci. Eng.: A 527 (21–22) (2010) 6064–6075.

[47] T. Seidel, A.P. Reynolds, Visualization of the material flow in AA2195 friction-stir welds using a marker insert technique, Metall. Mater. Trans. A 32 (11) (2001) 2879–2884.

[48] M. Song, R. Kovacevic, Numerical and experimental study of the heat transfer process in friction stir welding, Proc. Inst. Mech. Eng. Part B: J. Eng. Manuf. 217 (1) (2003) 73–85.

[49] D. Wang, B.L. Xiao, Q.Z. Wang, Z.Y. Ma, Evolution of the microstructure and strength in the nugget zone of friction stir welded SiCp/Al–Cu–Mg composite, J. Mater. Sci. Technol. 30 (1) (2014) 54–60.

[50] M. Azizieh, A. Kokabi, P. Abachi, Effect of rotational speed and probe profile on microstructure and hardness of AZ31/Al2O3 nanocomposites fabricated by friction stir processing, Mater. Des. 32 (4) (2011) 2034–2041.

[51] A. Sittiho, V. Tungala, I. Charit, R.S. Mishra, Microstructure, mechanical properties and strengthening mechanisms of friction stir welded Kanthal APMT™ steel, J. Nucl. Mater. 509 (2018) 435–444.

[52] A. Rollett, F. Humphreys, G.S. Rohrer, M. Hatherly, Recrystallization and Related Annealing Phenomena, Elsevier, 2004.

[53] K. Jata, S. Semiatin, Continuous dynamic recrystallization during friction stir welding of high strength aluminum alloys, Air force research lab wright-patterson AFB OH materials and manufacturing directorate, 2000.

[54] P.L. Threadgill, A.J. Leonard, H.R. Shercliff, P.J. Withers, Friction stir welding of aluminium alloys, Int. Mater. Rev. 54 (2) (2013) 49–93.

[55] C. Olea, L. Roldo, T. Strohaecker, J. Dos Santos, Friction stir welding of precipitate hardenable aluminium alloys: a review, Weld. World 50 (11–12) (2006) 78–87.

[56] S. Gatea, H. Ou, G. Mccartney, Deformation and fracture characteristics of Al6092/SiC/17.5p metal matrix composite sheets due to heat treatments, Mater. Charact. 142 (2018) 365–376.

[57] C. Olea, L. Roldo, J. Dos Santos, T. Strohaecker, A sub-structural analysis of friction stir welded joints in an AA6056 Al-alloy in T4 and T6 temper conditions, Mater. Sci. Eng.: A 454 (2007) 52–62.

[58] C. Marioara, S. Andersen, J. Jansen, H. Zandbergen, The influence of temperature and storage time at RT on nucleation of the β″ phase in a 6082 Al–Mg–Si alloy, Acta Mater. 51 (3) (2003) 789–796.

[59] R. Gupta, G. Chaudhari, B. Daniel, Strengthening mechanisms in ultrasonically processed aluminium matrix composite with in-situ Al3Ti by salt addition, Compos. Part B: Eng. 140 (2018) 27–34.

[60] C.-S. Kim, I. Sohn, M. Nezafati, J.B. Ferguson, B.F. Schultz, Z. Bajestani-Gohari, P.K. Rohatgi, K. Cho, Prediction models for the yield strength of particle-reinforced unimodal pure magnesium (Mg) metal matrix nanocomposites (MMNCs), J. Mater. Sci. 48 (12) (2013) 4191–4204.

[61] K. Kumar, H. Van Swygenhoven, S. Suresh, Mechanical behavior of nanocrystalline metals and alloys1, Acta Mater. 51 (19) (2003) 5743–5774.

[62] T. Mungole, P. Kumar, M. Kawasaki, T.G. Langdon, The contribution of grain boundary sliding in tensile deformation of an ultrafine-grained aluminum alloy having high strength and high ductility, J. Mater. Sci. 50 (10) (2015) 3549–3561.

[63] T. Srivatsan, A. Prakash, Effect of particulate silicon carbide on cyclic strain resistance and fracture behavior of X2080 aluminum alloy metal matrix composites, Eng. Fract. Mech. 49 (5) (1994) 751–772.

[64] T. Srivatsan, The low-cycle fatigue behaviour of an aluminium-alloy-ceramic-particle composite, Int. J. Fatigue 14 (3) (1992) 173–182.

[65] N. Chawla, Y.-L. Shen, Mechanical behavior of particle reinforced metal matrix composites, Adv. Eng. Mater. 3 (6) (2001) 357–370.

[66] V. Nardone, K. Prewo, On the strength of discontinuous silicon carbide reinforced aluminum composites, Scr. Metall. 20 (1) (1986) 43–48.

[67] Z. Zhang, Z. Wang, Grain boundary effects on cyclic deformation and fatigue damage, Prog. Mater. Sci. 53 (7) (2008) 1025–1099.

[68] R. Arsenault, L. Wang, C. Feng, Strengthening of composites due to microstructural changes in the matrix, Acta Metall. Mater. 39 (1) (1991) 47–57.

[69] Z. Zhang, D. Chen, Consideration of Orowan strengthening effect in particulate-reinforced metal matrix nanocomposites: a model for predicting their yield strength, Scr. Mater. 54 (7) (2006) 1321–1326.